

# How many occupational radiation doses were received by medical personnel during an interventional radiology procedure? A simulation study using Monte Carlo GATE

S.H. Zuber<sup>1</sup>, N.I.A. Mohd Hijas<sup>2</sup>, M.F.R. Abdul Hadi<sup>2</sup>, N.A.A. Hashikin<sup>2\*</sup>

<sup>1</sup>Centre for Diagnostic, Therapeutic and Investigative Studies, Faculty of Health Sciences, Universiti Kebangsaan Malaysia, Kuala Lumpur, Malaysia

<sup>2</sup>School of Physics, Universiti Sains Malaysia, Penang, Malaysia

## ► Original article

## ABSTRACT

### \*Corresponding author:

Hashikin NAA, Ph.D.

E-mail: hashikin@usm.my

Received: July 2024

Final revised: May 2025

Accepted: July 2025

Int. J. Radiat. Res., January 2026;  
24(1): 135-142

DOI: 10.61186/ijrr.24.1.21

**Background:** This study aimed to assess the equivalent and effective doses received by medical personnel during an interventional radiology procedure. **Materials and Methods:** Monte Carlo GATE was used to obtain the radiation doses. The protection provided by two protective garments was also investigated. **Results:** The effective doses at LLAT and RAO30 projections were found to contribute high doses to the medical personnel, with rates varying between 0.5 to 2.0  $\mu$ Sv. On the other hand, PA projection produced the lowest effective dose, between 0.04 to 0.6  $\mu$ Sv. In the simulation, a 0.5 mm-thick protective garment reduced the effective dose to more than three times. At LLAT and RAO30 projections, the effective dose with no protection increased with variations of 3 to 9  $\mu$ Sv, while PA projection increased the effective dose with variations of 1 to 3  $\mu$ Sv per procedure. **Conclusion:** A higher overall effective dose was observed for unshielded medical personnel. This work demonstrates the potential of Monte Carlo GATE in validating the doses received by medical personnel during interventional procedures.

**Keywords:** occupational exposure, personnel, Monte Carlo method, interventional radiology, protective devices.

## INTRODUCTION

In interventional radiology, the number of modalities and trained interventional radiologists has increased <sup>(1)</sup>, especially due to the increased awareness of the important role played by interventional radiology in medical practices. This is a distinct clinical discipline with its own training pathway <sup>(2)</sup>. However, its occupational hazards have been highlighted, with more medical personnel performing interventional radiology procedures being exposed to unnecessary radiation because the rapid developments in recent years do not correspond to the number of specialists. A lack of expertise has caused an absence of separation between neuro-interventionalists and body interventionalists, requiring them to undertake both procedures <sup>(1)</sup>.

Most interventional procedures are done in longer fluoroscopic time <sup>(3,4)</sup> due to their complexity, which contributes to the increasing radiation intensity experienced by patients and staff. Researchers have reported that fluoroscopic-guided interventional radiology is rapidly becoming more complex with the development of multiple new devices and procedures, including endografts to treat abdominal aortic aneurysms and vertebroplasty <sup>(5)</sup>. During the interventional procedures, radiologists are considered to be among the medical personnel who are exposed earliest to radiation as they must

perform the procedure close to the beam, where the scattered photon field from the equipment and the patient is high.

Many studies have been conducted to assess the clinical situation during these procedures, with one of the methods used being the Monte Carlo simulation. In medical physics, Monte Carlo is a well-established method that can aid in designing medical imaging devices <sup>(6-8)</sup>, evaluate new implementations of image reconstruction algorithms, optimise scan protocols, and simulate radiation transport when calculating physical measurement is difficult or impossible <sup>(9)</sup>. Monte Carlo Geant4 Application for Tomographic Emission (GATE) builds upon Monte Carlo Geant4 <sup>(10-18)</sup>, a widely used toolkit for simulate particle interactions with matter. GATE simplifies the use of Geant4 by making it more user-friendly, and it is specifically tailored for applications in nuclear medicine, diagnostic imaging, radiotherapy, and radiation dosimetry studies <sup>(19)</sup>. It is widely recognised for its flexibility in simulating various radiation transport scenarios and experimental setups. In the context of fluoroscopy setups, GATE <sup>(15)</sup> can accurately simulate the X-ray source, beam-shaping filters, patient phantoms, and detector systems, providing realistic representations of the radiation environments.

Therefore, the current work focused on evaluating effective doses for medical personnel because the occupational dose received by medical personnel

must be monitored to verify compliance with legal dose limits and the efficiency of protective radiation measures. In this study, a lead apron and a thyroid shield were the simulated protective garments as they are the radiation shielding devices most frequently used by medical personnel to reduce exposure to scattered radiation. An interventional suite was created using the Monte Carlo tools since the Monte Carlo algorithm can also simulate absorbed doses, effective doses, and equivalent doses with great accuracy. The novelty of this work is the generation of command scripts tailored for GATE v9.4, which enables efficient automation of simulation setups in addition to reducing manual input and human error, as well as the utilisation of SpekPy to create energy spectra that are highly customisable to match the parameters required in the simulation. This feature is particularly valuable when addressing complex procedure.

## MATERIAL AND METHODS

### Geometry design for the intervention suite model

Approval from the Institutional Review Board (IRB) was not required as this work involved no human or animal subjects or patients. The intervention suite model was mainly modelled using Monte Carlo GATE v9.1 (France) and mainly based on the <sup>(20-22)</sup> geometrical clinical setup. First, the patient's body was represented by a rectangular phantom 100 cm in length, 32 cm in width, and 23 cm in thickness. The head was modelled as a sphere with a radius of 13 cm. The patient phantom was composed according to the International Commission on Radiation Units and Measurements (ICRU) tissue and positioned at (0.0, 0.0, 0.0). According to Abdelrahman et al., ICRU tissue has a density of 1 g/cm<sup>3</sup> and is composed of approximately 76.2 % oxygen, 11.1 % carbon, 10.1 % hydrogen, and 2.6 % nitrogen <sup>(22)</sup>. Next, the patient's operation table was simulated as a 200 × 60 × 10 cm<sup>3</sup> box made of Bakelite, with a density of 1.25 g/cm<sup>3</sup> and a composition of 5.7441% hydrogens, 77.4591% carbon, 16.7968% oxygen. The table was positioned at (0.0, 0.0, -20.8), 1 cm away from the patient.

A member of the medical personnel was represented by a computational International Commission on Radiological Protection (ICRP) 110 phantom, portraying an adult reference female. A computational phantom of the human body was utilised to assess the energy deposition in approximately 141 organs due to internal and external radiation exposure. This phantom was based on a computed tomography (CT) scan of a 43-year-old individual 167 cm in height and with a mass of 59 kg. The CT scan comprised 174 slices of 5 mm thickness for the head and trunk, and 43 slices of 20 mm thickness for the legs, with each slice consisting of 256 × 256 pixels. The voxel height for the reference

female phantom's height was reduced from 5.0 mm to 4.84 mm because the reference individual, named Laura, was taller. The three-dimensional voxel array representing the computational phantom (organised into columns, rows, and slices) was oriented as follows: the x-coordinates were represented by columns increasing from right to left, the y-coordinates were represented by rows increasing from front to back, and the z-coordinates were represented by slices increasing from the toes up to the vertex of the body. Table 1 lists the main characteristics of the adult reference computational phantom, while table 2 details their segmented volumes and resulting masses compared to the reference masses.

**Table 1.** Characteristics of the adult female reference computational phantom. This includes voxel volumes, masses and tissue voxels, and elemental compositions, based on ICRP standards. These parameters form the basis for accurate radiation transport simulation and dose estimation in computational dosimetry.

Property	Female Reference Phantom
Height (m)	1.63
Mass (kg)	60.0
Number of tissue voxels	3, 886, 020
Slice thickness (voxel height, mm)	4.84
Voxel in-plane resolution (mm)	1.775
Voxel volume (mm <sup>3</sup> )	15.25
Number of columns	299
Number of rows	137
Number of slices	346 (+2; additional slices of skin at the top and bottom)

**Table 2.** Segmented volumes and resulting masses compared to the reference masses. The table presents detailed anatomical data for each organ, including total volume (in cm<sup>3</sup>) and mass (in grams). These values are essential for accurate modeling in radiation transport and dose calculations.

Organs	Volume (cm <sup>3</sup> )	Mass (g)	Reference mass (g)
Adrenals	12.6	13.0	13.0
Blood	807.4	855.8	4100
Brain	1238.1	1300.0	1300.0
Eyes	511.9	500.0	500.0
Eye lenses	14.3	15.0	15.0
Gall bladder	0.4	0.4	0.4
Gall bladder wall	54.3	56.0	56.0
Gall bladder contents	44.4	45.8	48.0
Stomach wall	134.6	140.0	140.0
Stomach contents	221.2	230.0	230.0
Small intestine wall	576.9	600.0	600.0
Small intestine contents	269.2	280.0	280.0
Right colon wall	139.4	145.0	145.0
Right colon contents	153.8	160.0	160.0
Left colon wall	139.4	145.0	145.0
Left colon contents	76.9	80.0	80.0
Recto-sigmoid colon wall	67.3	70.0	70.0
Sigmoid colon contents	76.9	80.0	80.0
Heart	587.3	620.0	620.0
Kidneys	261.9	275.0	275.0
Liver	1333.3	1400.0	1400.0
Lungs	2300.8	950.0	950.0
Lymphatic tissue	76.8	79.1	600
Muscle tissue	16,666.7	17,5000.0	17,500.0
Oesophagus	34.0	35.0	35.0
Ovaries	10.6	11.0	11.0
Skin	2496.8	2721.5	2300.0
Skeleton	5767.4	7760.1	7760.0
Spleen	125.0	130.0	130.0
Thymus	19.4	20.0	20.0
Thyroid	16.4	17.0	20.0
Uterus	77.7	80.0	80.0

The medical personnel representation was positioned 15 cm from the waist level of the patient, centred at  $(x = 15.0, y = 49.8, z = 0.0)$ , and then placed behind a 0.5 mm-thick lead apron and thyroid shield,  $100 \times 60 \text{ cm}^2$  and  $11 \times 7 \text{ cm}^2$  in size, respectively. The lead gown was modelled to cover the torso down one-third of the leg of the medical personnel, while the thyroid shield protected the thyroid area. Both protective garments had a density of  $11.35 \text{ g/cm}^3$  of tungsten, lead, and barium. The lead gown and thyroid shield were then removed to observe the absorbed dose received by every organ of the phantom when the protective garments were not worn, which enabled the effectiveness of the shielding to be determined. A geometry shaped as a rectangular box covering the phantom and known as *GlobalVol* was introduced to avoid any disturbance to the algorithm calculation. Figure 1 shows three different views of the geometry designed for the interventional suite.

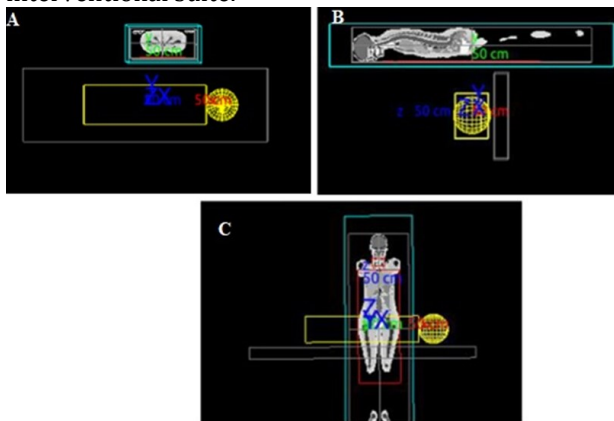


**Figure 1.** Three views of the geometry setup with the ICRP phantom in the green box as medical personnel and the geometric phantom in the yellow box as the patient; (a) top view; (b) lateral view; (c) front view.

### Projection design and x-ray spectra

In this study, three different patient exposure angles were investigated: posterior-anterior (PA), right anterior oblique,  $30^\circ$  (RAO30), and left lateral (LLAT). These projections were determined by<sup>(20)</sup> as the most commonly used source projections in coronary angiography. SpekPy, a toolbox designed to simulate X-ray tube spectra, was developed using the Python programming language (Python Software Foundation, DE, USA). At all the projections, the beams were modelled using the SpekPy v2.0.5 toolkit, which was centred on the patient's heart. The source position is defined in Table 3. The default X-ray beam of the SpekPy had an area of  $1 \text{ cm}^2$ , so the beams were defined to 25 degrees each to produce a cone-shaped X-ray beam.

### Effective dose Calculation

The simulations were conducted using one million photon histories to ensure statistical errors remained within acceptable limits. Accordingly, the photon was distributed to the patient phantom, while the medical

personnel received the scattered photon. When the simulation was completed, the system provided the output dose received by the 141 organs that were defined in their respective ID organs. From the absorbed dose generated by the system, the equivalent dose for all the organs can be calculated. According to ICRP 103, the equivalent dose can be calculated by multiplying the mean absorbed dose by the radiation weighting factor (WR). Since the photon was used as the source,  $WR = 1$ . To determine the effective dose received by medical personnel, the calculated equivalent doses were multiplied by their corresponding tissue weighting factors. The effective dose is a descriptor that characterises the radiation exposure to the medical personnel. In this study, descriptive statistics or exploratory data analysis (EDA) was deployed to evaluate the occupational radiation exposure received by the medical personnel and the effectiveness of the lead apron in reducing the exposure to scattered radiation.

**Table 3.** Source positions for the X-ray projections used in the simulation setup. Each entry specifies the spatial coordinates and angles of the X-ray source relative to the phantom, representing different clinical imaging views. These positions are critical for simulating realistic radiation exposure scenarios and dose distribution patterns.

	P	RAO30	LLAT
<b>x</b>	39.0	39.0	33.0
<b>y</b>	-15.0	5.0	-75.8
<b>z</b>	-74.6	64.5	0.87

PA: posterior-anterior, RAO30: right anterior oblique  $30^\circ$ , LLAT: left lateral.

## RESULTS

Figure 2 illustrates the poly-energetic X-ray spectra generated at different tube voltages (80.9 kVp, 85.7 kVp, and 116.0 kVp) using the SpekPy toolkit. The spectra reflect the energy distribution of the X-ray photons produced at each specified tube voltage, which shows how the X-ray photon energy changed as the tube voltage was raised. At 80.9 and 85.7 kVp, the X-ray spectrum demonstrated a relatively lower energy range, whereas at 116.0 kVp, a broader range of higher-energy X-rays was observed. Table 4 records the fluence intensity generated by SpekPy, with a higher tube voltage demonstrating higher fluence intensity.

**Table 4.** Fluence intensity per mAs per energy generated from SpekPy, used to model the input radiation details for dose calculation in computational simulations.

Tube voltage (kVp)	Fluence intensity (photons/cm <sup>2</sup> /mAs/keV)
80.9	$1.25169 \times 10^{14}$
85.7	$1.44858 \times 10^{14}$
116.0	$2.86197 \times 10^{14}$

### Organ equivalent doses

Tables 5 and 6 show the radiation received by the organs at the respective tube voltage and beam projections with and without protective garment.

**Table 5.** Organ equivalent doses ( $\mu\text{Sv}$ ) of the shielded medical personnel, with statistical uncertainty in parentheses.

Tube voltage (kVp)	LLAT	PA	RAO30
<b>Ovaries</b>			
80.9	0.00 (1)	0.00 (1)	0.00 (1)
85.7	0.00 (1)	0.00 (1)	0.00 (1)
116	0.00 (1)	0.00 (1)	0.2677 (0.9717)
<b>Bone surface</b>			
80.9	0.7167 (1)	0.1483 (1)	0.16331 (1)
85.7	0.1949(1)	0.5324 (0.9912)	1.68444 (1)
116	0.00 (1)	0.4273 (0.9925)	0.00 (1)
<b>Bladder</b>			
80.9	0.00 (1)	0.00 (1)	0.00 (1)
85.7	0.00 (1)	0.00 (1)	0.00 (1)
116	0.00 (1)	0.00 (1)	0.00 (1)
<b>Bone marrow (red)</b>			
80.9	0.5212 (1)	3.7527(0.9868)	0.8625 (0.9620)
85.7	0.9024(1)	0.8774 (0.9971)	2.1873 (0.9656)
116	0.4955 (1)	0.2285 (0.9974)	0.1755 (1)
<b>Brain</b>			
80.9	0.00(1)	0.00 (1)	0.00 (1)
85.7	0.00 (1)	0.00 (1)	0.00(1)
116	0.00 (1)	0.00 (1)	0.00 (1)
<b>Breast</b>			
80.9	4.0067(0.7888)	0.00 (1)	8.0143 (0.5797)
85.7	0.4563 (1)	0.00 (1)	0.00 (1)
116	0.00 (1)	0.00 (1)	1.0607(0.7115)
<b>Colon</b>			
80.9	0.00 (1)	0.00 (1)	0.00 (1)
85.7	0.00(1)	0.00 (1)	0.00 (1)
116	0.00 (1)	0.00 (1)	12.5261 (1.0909)
<b>Liver</b>			
80.9	0.00 (1)	0.00 (1)	0.00 (1)
85.7	0.00 (1)	0.00 (1)	0.00 (1)
116	0.00 (1)	0.00 (1)	0.00 (1)
<b>Lungs</b>			
80.9	0.00 (1)	0.00 (1)	0.00 (1)
85.7	0.00 (1)	0.00 (1)	0.00 (1)
116	0.00 (1)	0.00 (1)	0.00 (1)
<b>Oesophagus</b>			
80.9	0.00 (1)	0.00 (1)	0.00 (1)
85.7	0.00 (1)	0.00 (1)	0.00 (1)
116	0.00 (1)	0.00 (1)	0.00 (1)
<b>Salivary glands</b>			
80.9	0.00 (1)	0.00 (1)	0.00 (1)
85.7	0.00 (1)	0.00 (1)	0.00 (1)
116	0.00 (1)	0.00 (1)	0.00 (1)
<b>Skin</b>			
80.9	2.6090(0.8487)	16.5102(0.8806)	5.0108(1)
85.7	0.00 (1)	0.5521 (0.9640)	2.6217(1)
116	1.0187 (1)	0.8255 (0.8934)	1.39(0.9414)
<b>Stomach</b>			
80.9	0.00(1)	0.00 (1)	0.00 (1)
85.7	0.00 (1)	0.00 (1)	0.00 (1)
116	0.00 (1)	0.00 (1)	0.00 (1)
<b>Thyroid</b>			
80.9	0.00 (1)	0.00(1)	0.00 (1)
85.7	0.00 (1)	0.00 (1)	0.00 (1)
116	0.00 (1)	0.00 (1)	0.00 (1)
<b>Remainder</b>			
80.9	0.0861(0.9914)	0.0701(0.9810)	0.00(1)
85.7	0.0958(0.9921)	0.4314(0.9831)	0.2187(0.9843)
116	3.2098(0.9944)	0.0491 (0.98298)	8.78121(1)

PA: posterior-anterior, RAO30: right anterior oblique 30°, LLAT: left lateral.

**Table 6.** Organ equivalent doses ( $\mu\text{Sv}$ ) received by the unshielded medical personnel, with statistical uncertainty in parentheses.

Tube Voltage (kVp)	LLAT	PA	RAO30
<b>Ovaries</b>			
80.9	54.3758 (1)	0.00 (1)	0.00 (1)
85.7	0.00 (1)	0.00 (1)	0.00 (1)
116	0.00 (1)	7.1819 (1)	0.00 (1)
<b>Bone surface</b>			
80.9	3.1267(0.9678)	1.9680(0.9884)	3.7879(0.9535)
85.7	2.9811(0.9931)	0.72060(1)	0.1633 (1)
116	2.5047(0.9918)	0.4585(0.9928)	1.4842(0.9774)
<b>Bladder</b>			
80.9	10.2426(1)	23.2380(1)	0.00 (1)
85.7	0.00(1)	0.00(1)	0.00 (1)
116	0.00(1)	0.00(1)	0.00 (1)
<b>Bone marrow (red)</b>			
80.9	4.5598(0.9299)	1.0647(0.9902)	6.0458(0.9177)
85.7	1.6823 (0.9943)	2.7864(0.9897)	1.0004(0.9620)
116	3.2557 (0.9794)	1.2391(1)	4.0254(0.9972)
<b>Brain</b>			
80.9	3.3365 (0.8775)	1.81097(1)	12.782(0.5645)
85.7	0.00 (1)	0.00(1)	0.00(1)
116	0.47065(1)	0.00(1)	5.9987(0.8546)
<b>Breast</b>			
80.9	0.4321(0.9267)	2.9659(1)	27.6521(0.9120)
85.7	5.2048(0.9165)	0.92696(1)	8.0143(0.5797)
116	3.8857(1)	0.4563(1)	24.098(0.9665)
<b>Colon</b>			
80.9	16.8517(1.0072)	0.00(1)	1.8260(1.0909)
85.7	5.0758(1.0909)	0.5804(1.0909)	0.00(1)
116	11.9700(1.0909)	0.59923(1)	0.00(1)
<b>Liver</b>			
80.9	22.2651(0.8785)	8.9694(0.5568)	9.3986(0.5917)
85.7	7.7562(0.5310)	0.42374(1)	0.00(1)
116	7.4692(0.5255)	0.00(1)	10.0960(0.8750)
<b>Lungs</b>			
80.9	0.2375(0.8131)	0.5407(1)	13.3177(0.7632)
85.7	4.1086(1)	3.8977(0.9485)	0.00(1)
116	7.4423(0.9014)	0.3141(1)	7.5035(0.9022)
<b>Oesophagus</b>			
80.9	0.00(1)	0.00(1)	0.00(1)
85.7	0.00(1)	0.00(1)	0.00(1)
116	0.00(1)	0.00(1)	0.00(1)
<b>Salivary glands</b>			
80.9	0.00(1)	0.00(1)	36.7352(1)
85.7	0.00(1)	0.00(1)	0.00(1)
116	0.00(1)	2.40399(1)	0.00(1)
<b>Skin</b>			
80.9	3.6889(0.7833)	3.6646(0.7920)	0.5105(0.8896)
85.7	5.5642(0.8647)	2.3132(0.7335)	5.0108(1)
116	3.5809(0.8094)	1.0187(1)	3.6703(0.9118)
<b>Stomach</b>			
80.9	0.2052(1)	0.00(1)	0.00(1)
85.7	0.00(1)	0.00(1)	0.00(1)
116	0.00(1)	0.00(1)	0.00(1)
<b>Thyroid</b>			
80.9	0.00(1)	0.00(1)	10.8771(0.8111)
85.7	0.00(1)	0.00(1)	0.00(1)
116	0.00(1)	0.00(1)	10.1842(0.8750)
<b>Remainder</b>			
80.9	5.5937(0.9067)	13.3244(0.9674)	3.411(0.9434)
85.7	6.5980(0.9537)	0.4488(0.9591)	0.0096(0.9921)
116	2.5781(0.9305)	3.4022(0.9673)	3.9283(0.9748)

PA: posterior-anterior, RAO30: right anterior oblique 30°, LLAT: left lateral.

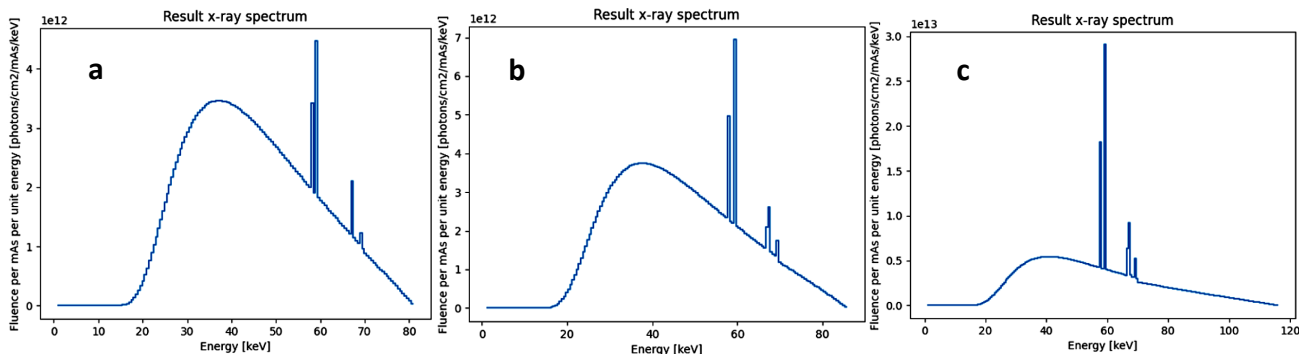


**Figure 2.** Poly-energetic X-ray spectrum generated at (a) 80.9 kVp; (b) 85.7 kVp; (c) 116.0 kVp, an essential input for accurate simulation of radiation interactions in computational dosimetry models.

Table 5 and 6 demonstrate that at LLAT projection, a high equivalent dose was recorded for the breast and skin at 80.9 kVp, whereas at PA projection, a high equivalent dose was recorded for the skin, as received by the shielded medical personnel. At 87.5 kVp, a generally small organ equivalent dose was observed. At 116.0 kVp, a high organ equivalent dose was observed in the colon at RAO30 projection.

The results also demonstrated high organ equivalent dose for sensitive organs such as ovaries at LLAT projection, bladder at PA projection, breast and salivary glands at RAO30 projection, received by unshielded medical personnel at 80.9 kVp. At 85.7

kVp, high organ equivalent dose can be observed breast, colon, liver and skin at LLAT projection, whereas at 116.0 kVp, highest dose can be observed at breast in RAO30 projection.

### Effective dose of medical personnel

The calculated effective doses received by the medical personnel with and without shielding are shown in figure 3. Figures 3 and 4 illustrate high overall effective doses for all projections received by medical personnel without personal garment as compared to with protective garment. Figure 4 shows the effective dose with and without using protective garment at different kVp energies.

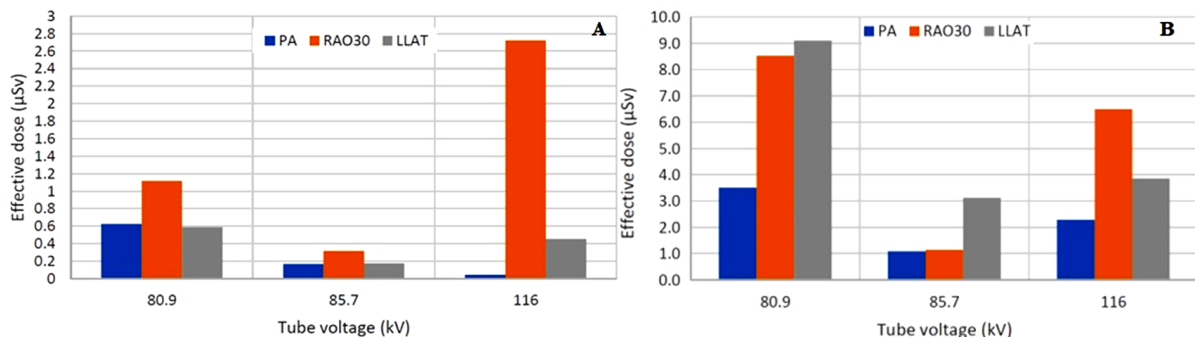


**Figure 3.** Effective dose at three different projections (a) using protective garments; (b) without using protective garments.

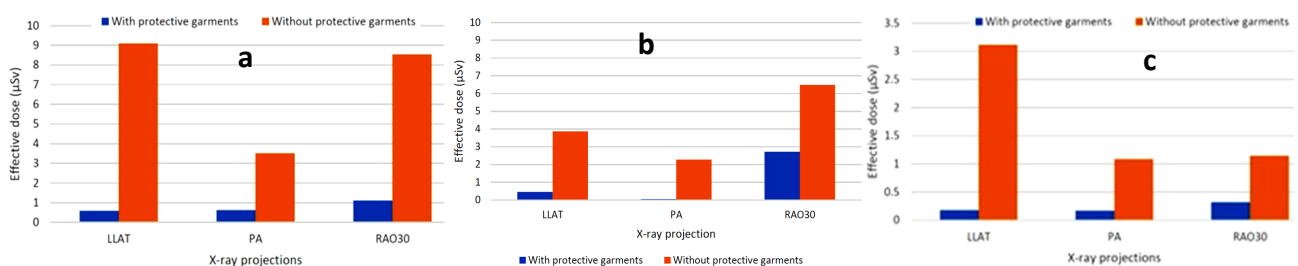


**Figure 4.** Comparison of effective dose with and without using protective garment at (a) 80.9 kVp; (b) 85.7 kVp; (c) 116.0 kVp.

## DISCUSSION

The results demonstrate that the SpekPy could produce X-ray energies from the tungsten target used, in keV, against the fluence per unit energy (photons/cm<sup>2</sup>/mAs/keV), as shown in table 4. The poly-energetic X-ray beam was created where each X-ray photon carries its own discrete energy. The spectral intensity was described by the energy

fluence. Meanwhile, the peak energy of the X-ray spectrum represented the peak kilovoltage applied to the tube, and the mean energy of the peak was about one-third to one-half of the spectrum<sup>(23)</sup>.

The results in tables 5 and 6 clearly show that more organs attenuate radiation, which contributes to a higher occupational radiation dose. The magnitude of equivalent doses for the organs was influenced by various factors, such as tube voltage,

organ size, and the position of the organs relative to the beam projections<sup>(20)</sup>. When the tube voltage was increased, the X-ray energy from the source was higher, which caused the penetration ability to increase as well. Thus, less attenuation of radiation by the organs occurred since the radiation was transmitted by passing through the body. This might also have occurred because the scattered radiation did not evenly attenuate with other materials, such as the operation table or the protective garments, before it could be received by the medical personnel. A previous work<sup>(24)</sup> described how fluoroscopic imaging results in a radiation field that is unevenly distributed throughout the suite. The radiation field becomes more asymmetrical as the gantry rotates, which may increase the radiation doses<sup>(24)</sup>.

Another factor may be the size of the organs themselves. Organs that are more evenly distributed throughout the body, such as the bone marrow and skin, receive higher radiation doses under all beam source conditions. In contrast, the equivalent dose for localised organs, such as the breast or other specific organs, varies depending on the source projections. The results also indicated that some organs have different attenuations of radiation despite being considered to be the same tissue type or have the same tissue density. For example, the liver and lungs are considered soft tissues. This is because the volume, composition, and mass of the reference organs are different to those that eventually contribute to different mass absorption coefficients<sup>(25)</sup>.

The results also illustrate the comparison between the equivalent dose when the protective garments were worn and when they were not. When the medical personnel were shielded, most of the critical organs did not even receive radiation, and this attenuated after reaching the skin. The shielding effect of the protective garments helped absorb the radiation before it passed through the critical organs. Radiation-induced skin damage is an uncommon complication of interventional procedures. However, it can sometimes occur due to the cumulative dose from repeated diagnostic procedures<sup>(26)</sup>.

The position of the X-ray source is also an essential factor in the medical personnel's equivalent doses. Organs closer to the source may receive higher radiation doses, particularly from lower energy photons, as scattered radiation deposits a larger portion of its energy in shallow organs like the breast and skin<sup>(20)</sup>. The figures indicate that the organ equivalent doses were higher at RAO30 and LLAT projections since the source radiated more directly towards the medical personnel. Compared to PA projections, the beams could attenuate with the table and patient before being scattered. In coronary angiography or percutaneous coronary intervention (PCI), where medical personnel must stand closer to the irradiated area, the radiation dose is higher

compared to procedures like transjugular intrahepatic portosystemic shunt (TIPS), which uses the femoral access route<sup>(26)</sup>.

As shown in figure 3, the effective dose received by the medical personnel was high at 80.9 kVp, but it decreased when the tube voltage was increased to 85.7 kVp. This may have happened because even though the tube voltage was increased, the tube current and fluoroscopy time of the interventional procedure decreased from 730 mA to 350 mA. In clinical imaging, a high tube voltage setup is compensated for by a lower tube exposure to reduce the patient's exposure to radiation, so less scattered radiation would be received by the medical personnel. Increasing the tube current (mA) resulted in a greater production of electrons in the X-ray tube, thereby increasing the quantity of X-rays generated. More radiation means that more photons will be heated and collide with the target to produce radiation<sup>(23)</sup>. The fluoroscopy time measures the electron production in the tube and how long the exposure will last. At 80.9 kVp, the fluoroscopy time was 7.47 min, far higher than the fluoroscopy time at 85.7 kVp. Thus, prolonging the fluoroscopy time contributed to the higher effective dose received by the medical personnel. When the tube voltage was increased again from 85.7 kVp to 116.0 kVp, the effective dose also increased again; however, it was much lower than the effective dose at 80.9 kVp since the tube current (120 mA) was at its lowest at 116.0 kVp and with a fluoroscopy time of 12.4 min.

Moreover, the material of the operational table (Bakelite) might also have affected the scattered radiation emitted from PA projections. Polymers including Bakelite have shown high mass attenuation coefficients and the capacity to become good shielding materials, between 59.5 - 1332.5 keV. They not only exhibit superior radiation resistance but also possess thermal stability and high mechanical properties<sup>(27)</sup>. Thus, since PA beams attenuated from the table and patient, the radiation received by the medical personnel was reduced. Based on Figure 4, when protective garments were not worn, the effective dose at each kVp setup increased more than threefold compared to when they were worn. For example, at LLAT projections, the value of the effective dose at 80.9 kVp increased from 0.5869  $\mu$ Sv to 9.097  $\mu$  Sv. Arguably, therefore, the model realistically depicts the no-apron case during an interventional procedure.

The effective dose reduction when the 0.5 mm-thick lead gown was worn occurred because of the decreased backscattered radiation from the medical personnel's body. The X-rays were significantly attenuated by the lead before they could be fully absorbed by the body. Lead aprons and thyroid shields offer the best protection when scattered radiation consists of a relatively soft spectrum, resulting from large-angle scattering or low tube

voltage<sup>(9)</sup>. At LLAT projection, the higher effective dose at 116.0 kVp may be attributed to the ability of energetic photons to penetrate the apron more easily than lower energy photons at lower tube voltages. Consequently, at high kVp, the apron was less effective at providing optimal protection.

Regardless of the apron, the over-couch X-ray tube position of RAO30 and LLAT during cardiological procedures resulted in the highest effective doses. During these projections, more scattered radiation penetrated the middle and upper portions of the body trunk, where most radiosensitive organs are located. However, for the under-couch position PA, absorption in the patient's trunk filtered the X-ray beam, resulting in a harder energy spectrum in the transmitted radiation. As a result, the radiation intensity was much lower than at the other projections, leading to relatively lower effective doses being received by the medical personnel.

One limitation of this work is that the simulation does not accurately represent a dedicated fluoroscopy room with specific measurements. This could impact its accuracy as the dimensions and layout of a real fluoroscopy room, including the walls, shielding, and distance between the X-ray source, patient, and medical personnel, play crucial roles in photon interactions. The lack of a detailed representation of the enclosed space means that factors such as scatter radiation and attenuation due to room materials may not be fully accounted for, potentially affecting the estimated overall dose distribution and occupational exposure during the fluoroscopy procedure.

## CONCLUSION

In this work, the medical personnel were exposed to the highest radiation at LLAT and RAO30 projections, with significant doses affecting the breast, skin, and bone marrow, with a higher overall effective dose being observed in the unshielded medical personnel. In contrast, mild primary projections such as PA moderately impacted the dose levels. This study demonstrates how Monte Carlo GATE can effectively validate the equivalent and effective doses received by medical personnel during such procedures.

**Acknowledgement:** The authors thanked the School of Physics, Universiti Sains Malaysia for allowing this work to be conducted. The authors also acknowledged the Ministry of Higher Education Malaysia for Fundamental Research Grant Scheme (FRGS/1/2019/STG02/USM/02/2) for the financial support. AI was employed to rephrase the paragraph for overall improvement.

**Conflict of interest:** None. The authors declare that they have no known competing financial interests or

personal relationships that could have appeared to influence the work reported in this paper.

**Funding:** Ministry of Higher Education Malaysia (MOHE), Fundamental Research Grant Scheme (FRGS/1/2019/STG02/USM/02/2).

**Ethical consideration:** None

**Authors' Contribution:** H.F., I. participate in the conceptualisation, data curation, formal analysis, investigation and validation. Funding acquisition, supervision and software contribution are led by H. H. and I. participate in writing dan visualisation of the whole manuscript.

## REFERENCES

1. Abdullah BJJ (2009) State and future of interventional radiology in Malaysia. *Biomed. Imaging Interv J*, **5**(4): e33.
2. Brock KK, Chen SR, Sheth RA, Siewerdsen JH (2023) Imaging in interventional radiology: 2043 and beyond. *Radiology*, **308**: e230146.
3. Chida K, Takahashi T, Ito D, et al. (2011) Clarifying and visualizing sources of staff-received scattered radiation in interventional procedures. *Am J Roentgenol*, **197**: W900-3.
4. León-Salas B, Infante-Ventura D, Hernandez-Yumar A, et al. (2025) Conduction system pacing using electro-anatomical mapping-guided system vs. fluoroscopy: a systematic review, meta-analysis and economic evaluation. *Front Cardiovasc Med*, **11**: 1519127.
5. Chida K, Kaga Y, Haga Y, et al. (2013) Occupational dose in interventional radiology procedures. *Am J Roentgenol*, **200**: 138-141.
6. Abdelrahman M, Lombardo P, Dabin J, Struelens L, Vanhavere F (2023) Impact of the implementation of the new radiation quantities recommended by ICRU/ICRP for practical use in interventional radiology: a Monte Carlo study. *J Radiol Prot*, **43**: 11513.
7. Balcaza VG, Camp A, Sánchez RM, Ginjaume M, Duch MA (2023) Dose assesment with fast Monte Carlo codes in interventional radiology. *Radiat Prot Dosimetry*, **199**: 1813-1817.
8. Yanagawa A, Takata T, Onimaru T, et al. (2023) New perforated radiation shield for anesthesiologists: Monte Carlo simulation of effects. *J Radiat Res*, **64**: 379-386.
9. Siiskonen T, Tapiovaara M, Kosunen A, Lehtinen M, Vartiainen E (2007) Monte Carlo simulations of occupational radiation doses in interventional radiology. *Br J Radiol*, **80**: 460-468.
10. Limbaco ME, Toledo FU, Tondo RMV, Nawang SA (2025) Modelling and validation of a 6 MV compact linear accelerator via Monte Carlo simulation using Geant4 application for tomographic emission (GATE). *Biomed Phys Eng Express*, **11**: 25018.
11. Buvat I and Lazaro D (2006) Monte Carlo simulations in emission tomography and GATE: An overview. *Nucl Instruments Methods Phys Res Sect A Accel Spectrometers Detect Assoc Equip*, **569**: 323-329.
12. Haghghat Nazar N, Firoozabadi MM, Ghorbani M. (2025) Improving dose accuracy in radiation therapy: Validating monte carlo simulations with GATE and PRIMO. *Thums-JMS*, **12**: 79-89.
13. Kaddouch S and El Khayati N (2025) Dose coefficients of ICRP adult reference voxel phantom for internal dosimetry of selected radiopharmaceuticals using Geant4/GATE simulation. *Radiat Prot Dosimetry*, **201**(7): 511-521.
14. Sarrut D, Bardiès M, Bousson N, et al. (2014) A review of the use and potential of the GATE Monte Carlo simulation code for radiation therapy and dosimetry applications.

*Med Phys*, **41**: 64301.

15. Nasr B, Villa M, Benoit D, Visvikis D, Bert J (2024) Monte Carlo dosimetry validation for x-ray guided endovascular procedures. *Ann Vasc Surg* **99**: 186-192.
16. Sabalza-Castillejo W, Martin-Landrove M (2025) Determination of the absorbed dose in the brain with DICOM images using GATE/GEANT4 and MATLAB. *arXiv Prepr*, arXiv2505.01970.
17. Sadremomtaz A and Mollae Bijarpasi F (2024) Evaluation of proton beam dose distribution in breast tissue based on GATE simulation code. *Frontiers in Biomedical Technologies*, **12**.
18. Zuber SH, Hadi MA, Hashikin NAA, et al. (2025) Dosimetric evaluation of brain radiotherapy using custom-made Rhizophora head phantom—comparison between Monte Carlo GATE and treatment planning system MONACO. *Int J Radiat Res*, **23**: 13-20.
19. Benameur Y, Tahiri M, Mkimel M, et al. (2023) Fetal dose estimation during pregnancy using Gate Monte Carlo simulation: application of Hodgkin's lymphoma radiotherapy. *Radiat Prot Dosimetry*, **199(7)**: 581-587.
20. Bozkurt A and Bor D (2007) Simultaneous determination of equivalent dose to organs and tissues of the patient and of the physician in interventional radiology using the Monte Carlo method. *Phys Med Biol*, **52**: 317-330.
21. Božović P, Ciraj-Bjelac O, Stanković-Petrović JS, Arandić D, Čeklić S (2018) Utilizing Monte Carlo simulations in estimation of occupational eye lens dose based on whole body dosimeter in interventional cardiology and radiology. *Nucl Technol Radiat Prot*, **33**, 375-379.
22. Abdelrahman M, Lombardo P, Camp A, et al. (2020) A parametric study of occupational radiation dose in interventional radiology by Monte-Carlo simulations. *Phys Medica*, **78**: 5870.
23. Dance DR, Christofides S, Maidment ADA, McLean ID, Ng KH (2014) Diagnostic radiology physics: A handbook for teachers and students. *American association of physicists in medicine, Asia-oceania federation of organizations for medical physics, European federation of organisations for medical physics*, Pp: 1-710.
24. Haqqani OP, Agarwal PK, Halin NM, lafrati MD (2013) Defining the radiation 'scatter cloud' in the interventional suite. *J Vasc Surg*, **58**: 1339-1345.
25. Mohammed SI and Taqi AH (2025) Mass attenuation coefficient of electromagnetic radiation for human tissues. *J Radiat Res Appl Sci*, **18**: 101255.
26. He W (2014) Monte carlo modeling based patient dose optimization in diagnostic radiology. *Clemson University ProQuest Dissertations & Theses*. **3636809**.
27. More CV, Alsayed Z, Badawi MS, Thabet AA, Pawar PP (2021) Polymeric composite materials for radiation shielding: a review. *Environ Chem Lett* **19**: 2057-2090.